

## RESEARCH ARTICLE

View Article Online  
View Journal | View IssueCite this: *Inorg. Chem. Front.*, 2026,  
13, 4521

# Diketopyrrolopyrrole organic cations as strategy for iodide and lead-free hybrid metal–halide based photoconductors

Théo Forestier,<sup>a</sup> Marcin Kielar,<sup>a</sup> Claudia Wilfinger,<sup>a</sup> Aseem Rajan Kshirsagar,<sup>b</sup> Mikaël Kepenekian,<sup>b</sup> Alexandre Abhervé<sup>✉</sup> and Flavia Pop<sup>✉</sup>

For the next generation of photoconductors, hybrid molecular materials based on metal–halide anionic networks and electroactive organic cations of viologen type have been considered. Charge-transfer hybrid materials with reasonable (photo)conducting responses required the association to lead-iodide based inorganic components. Here, the benefit of using an organic divalent cation based on the diketopyrrolopyrrole (DPP) chromophore afforded a series of iodide-free and one example of lead-free photoconducting devices. Specifically, lead-chloride and lead-bromide compounds present an electronic structure of type I with frontier orbitals based solely on the organic cation, while the bismuth-bromide 1D perovskite network reveals a type II alignment with participation of both components to the charge transfer. The resulting devices show relevant photocurrent/dark current response ratios of up to 3.7 at 1.0 mW mm<sup>-2</sup>, opening the strategy of DPP-based hybrid metal–halides for stable and non-toxic photoresponsive devices.

Received 2nd February 2026,

Accepted 1st April 2026

DOI: 10.1039/d6qi00231e

rsc.li/frontiers-inorganic

## Introduction

While halide perovskites have emerged as one of the most promising family of materials for solar cell technology,<sup>1</sup> the poor stability to moisture exposition of the iodide-based three-dimensional (3D) structure encouraged chemists to use large organic molecules as cations, resulting in two-dimensional (2D) or one-dimensional (1D) inorganic networks with enhanced stability.<sup>2</sup> Such compounds usually present a wide electronic bandgap, with no contribution of the organic part in the valence band maximum (VBM) or conduction band minimum (CBM), thus following a type-I alignment (VBM and CBM reside on the inorganic component).<sup>3</sup> Due to quantum and dielectric confinement of the charge carriers, these materials were mainly used for light-emitting or sensing devices,<sup>4</sup> and as photodetectors when associated to graphene in heterostructures.<sup>5</sup> On the other hand, an interesting strategy to reduce the electronic bandgap and afford optoelectronic functionalities is through electroactive cations that can trigger charge transfer (CT) in the hybrid metal–halide structure.<sup>6</sup> In this case, the organic moieties can be active and participate by

adjusting the edge energy levels of the material (bands arranged in a type-II alignment).<sup>7</sup> This strategy has been employed for the preparation of 2D hybrid perovskite structures with possible applications in solar cell, LED and FET devices,<sup>8</sup> as well as in 1D iodoplumbate networks thus affording photoconductivity.<sup>9,10</sup> A third option, less explored, consists in using the inorganic part to template the hybrid structure without being involved in the electronic edge states, leading to a type-I alignment with VBM and CBM on the organic part, in which case the band gap is controlled only by the energy levels of the organic cations.<sup>11</sup> Among electroactive cations, methylviologen (MV<sup>2+</sup>) was previously combined to group 15 metal ions (Bi<sup>III</sup> and Sb<sup>III</sup>)<sup>12–14</sup> or to lead-iodides in order to afford 1D CT hybrid semiconductors.<sup>15</sup> In the latter example, Fujisawa and Ishihara could highlight CT from the valence band of the anionic network to the LUMO (lowest unoccupied molecular orbital) of the organic cation, which was further confirmed by the support of density functional theory (DFT) based calculations, showing that the CBM consisted in the LUMO of MV<sup>2+</sup>.<sup>16</sup> More recently, new viologen derivatives bearing H-bonding functionality have been used in order to tune the bandgap *via* supramolecular organization, hence inducing photoconductivity.<sup>17</sup> On the other hand, Kanatzidis *et al.* recently used similar viologen cations while changing the composition of the inorganic network (Pb *vs.* Sn).<sup>18</sup> This solid solution approach represents an efficient way

<sup>a</sup>Univ Angers, CNRS, MOLTECH-Anjou, SFR MATRIX, F-49000 Angers, France.  
E-mail: alexandre.abherve@univ-angers.fr, flavia.pop@univ-angers.fr

<sup>b</sup>Univ Rennes, ENSCR, CNRS, ISCR – UMR 6226, F-35000 Rennes, France

to finely tune the bandgap. Nevertheless, the short absorption range of these viologen cations require the association with iodide-based inorganic networks, which are usually more unstable compared to their bromide and chloride-based congeners.<sup>19</sup> Another way to enhance CT and broaden the absorption spectra consists in changing the electronic character of the MV<sup>2+</sup> based derivatives while preserving a hydrogen bonding motif. Diketopyrrolopyrroles (DPPs) have become attractive for photoconducting materials due to their chemical versatility, solution processability, high absorption and fluorescence quantum yield.<sup>20–22</sup> Despite increased absorption and stability of the redox forms,<sup>23</sup> electron deficient DPP-pyridine-based monocations (DPP-Py<sup>1+</sup>) and dications (DPP-Py<sup>2+</sup>) have been very little studied so far, mostly as fluorescent probes<sup>24–27</sup> or for electrochromic displays.<sup>28</sup> On the other hand, a DPP-thiophene derivative bearing alkylammonium side chains was successfully inserted in a series of quasi-2D perovskite compounds for solar cell applications, although single-crystal X-ray structures couldn't be described.<sup>29</sup> Within this work we took advantage of the structural similarity between MV<sup>2+</sup> and DPP-Py<sup>2+</sup> dications (Fig. 1) to synthesize hybrid organic–inorganic metal–halide materials. Beside similar redox behavior, the DPP-Py<sup>2+</sup> has several advantages such as red-shifted absorption and impressive molar absorp-

tivity in the reduced states, two lactam units prone to hydrogen bonding and electron reductions at much negative potentials thanks to its electron acceptor core.<sup>19</sup> The direct consequence of its electron deficient character translates in lower LUMO energy and thus reduced band gap. We report herein several 1D organic–inorganic hybrid materials based on DPP-Py<sup>2+</sup> acceptor and Pb<sub>2</sub>X<sub>6</sub><sup>2–</sup> (X = Cl, Br, I) or BiBr<sub>5</sub><sup>2–</sup> as metal–halide donors. The effective small band gaps, confirmed by UV-Vis absorption measurements, photoelectron spectroscopy in air (PESA) and theoretical calculations, enabled the fabrication of pressed pellet-based photoconductors with interesting photocurrent/dark current response ratio.

## Results and discussion

### Synthesis and single-crystal X-ray structures

The desired DPP-Py<sup>2+</sup> dication was obtained stepwise as iodide and hexafluorophosphate salts from the DPP-4-pyridyl previously described (Scheme 1).<sup>31</sup> The iodine salt was obtained in good yields by using an excess of methyl-iodide in acetonitrile at 80 °C, whereas the hexafluorophosphate salt by counter anion exchange, similarly to previously reported DPP-hexylPy<sup>2+</sup> dication.<sup>19</sup>

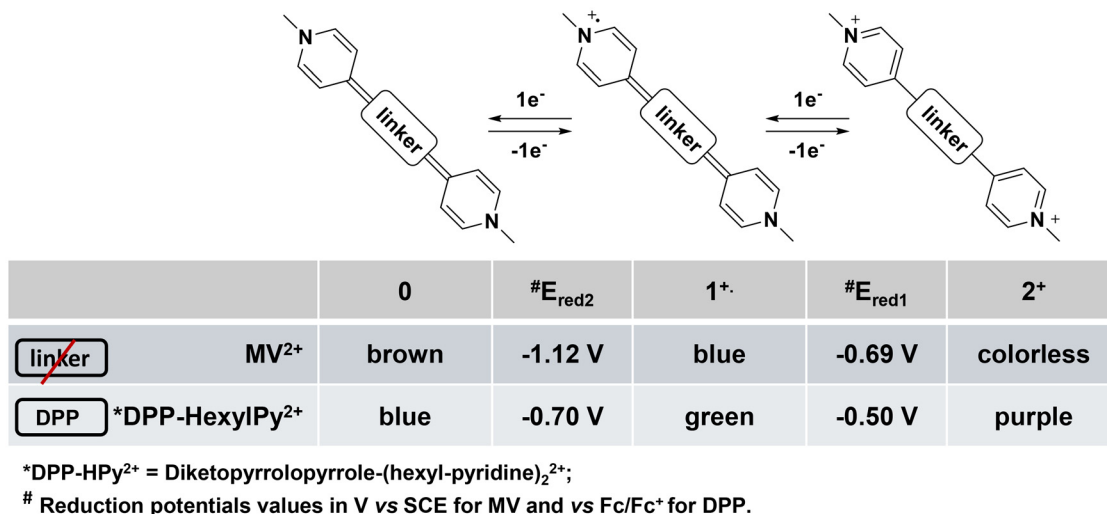
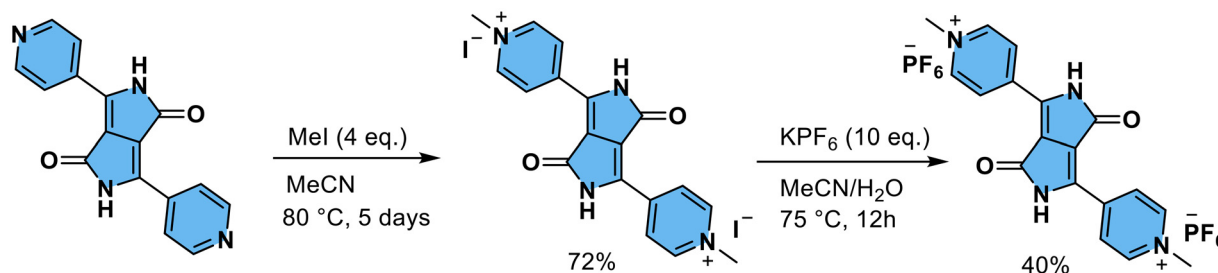


Fig. 1 Redox properties of MV<sup>2+</sup> and DPP-hexylPy<sup>2+</sup> dications.



Scheme 1 Synthesis of DPP-Py<sup>2+</sup> dications as iodide and hexafluorophosphate salts.

Subsequently, the synthesis of the hybrid compounds was carried out by mixing one equivalent of the cation salt with one equivalent of the metal halide salt under stirring and heating in HX (X = Cl, Br, I). While the lead-chloride and lead-bromide hybrid compounds of general formula (DPP-Py)Pb<sub>2</sub>X<sub>6</sub> could be crystallized as black needles, the reaction of the cation with HI under heating resulted in the hydrogenation of the DPP core and breaking of the aromaticity, affording non-conjugated H<sub>4</sub>DPP-Py dications and Pb<sub>3</sub>I<sub>12</sub> cluster anions (Fig. S2). Therefore, another strategy was adopted for the reaction with PbI<sub>2</sub>, using either DMF or DMSO as a solvent and stoichiometric amount of HI. Following this procedure, the two compounds of formula (DPP-Py)Pb<sub>2</sub>I<sub>6</sub>(DMF)<sub>2</sub> and (DPP-Py)Pb<sub>2</sub>I<sub>6</sub>(DMSO)<sub>2</sub> could be obtained as black needle-like and platelet-like crystals, respectively. Two more 1D lead-bromide compounds of formula (H<sub>x</sub>O<sub>y</sub>)(DPP-Py)<sub>2</sub>Pb<sub>2</sub>Br<sub>9</sub> could be obtained starting from (DPP-Py)I<sub>2</sub> instead of (DPP-Py)(PF<sub>6</sub>)<sub>2</sub>. A non-perovskite single-chain network (mix of corner and edge-sharing octahedra; x = 13, y = 6) was obtained as black platelet-like crystals (Fig. S3 and S4), while the brown needles corresponded to a perovskite-type network (double chains of corner-sharing octahedra; x = 9, y = 4, Fig. S3, S5 and S6). These two compounds are solvatomorphs since they only differ in their formula by the number of water solvent molecules in the hydronium cluster. Finally, replacing PbBr<sub>2</sub> by BiBr<sub>3</sub> afforded the lead-free 1D perovskite network of formula (DPP-Py)BiBr<sub>5</sub> as black needle-like crystals.

(DPP-Py)Pb<sub>2</sub>Cl<sub>6</sub> and (DPP-Py)Pb<sub>2</sub>Br<sub>6</sub> are isostructural and crystallized in the monoclinic space group *P*2<sub>1</sub>/*n*. The hybrid compounds are made of column stacks of organic DPP molecules and a very peculiar 1D inorganic chain. Indeed, the unusual seven-coordination of the metal ion results in chains of monocapped trigonal prisms with face-sharing and edge-sharing connectivity (Fig. 2). Only one example of this type of 1D network has previously been obtained by Lightfoot *et al.* using imidazolium and 4-methylimidazolium cations with lead-bromide.<sup>32</sup> Otherwise, this rare architecture has mainly been observed in 2D lead-halide networks of general formula APb<sub>2</sub>X<sub>5</sub> where the 1D chains of monocapped prisms are interconnected to form corrugated layers.<sup>33–35</sup> In both cases, the seven-coordination in lead-chloride and lead-bromide hybrids has always been obtained using secondary amine precursors, showing the role of hydrogen bonding.<sup>36</sup> Indeed, the strongest intermolecular interactions between organic cation and inorganic network in (DPP-Py)Pb<sub>2</sub>X<sub>6</sub> compounds don't involve the methyl-pyridinium but rather the pyrrole units, as highlighted by the short N–H...Cl and N–H...Br distances (with N...Cl and N...Br distances of 3.189 and 3.362 Å, respectively, see Fig. S7). Finally, the cation stacks show strong  $\pi$ – $\pi$  stacking with a short distance between DPP units of 4.019 and 4.145 Å corresponding to the crystallographic *a* parameter in (DPP-Py)Pb<sub>2</sub>Cl<sub>6</sub> and (DPP-Py)Pb<sub>2</sub>Br<sub>6</sub>, respectively.

In both (DPP-Py)Pb<sub>2</sub>I<sub>6</sub>(DMF)<sub>2</sub> and (DPP-Py)Pb<sub>2</sub>I<sub>6</sub>(DMSO)<sub>2</sub> compounds, the inserted solvent molecule strongly interacts with the pyrrole unit of the DPP-Py cation (Fig. 3). Therefore, the intermolecular interactions between cation and inorganic

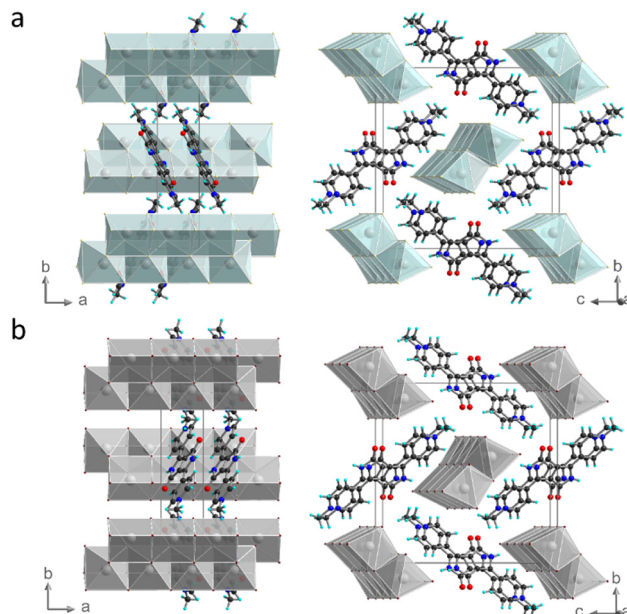


**Fig. 2** Crystal structures of (a) (DPP-Py)Pb<sub>2</sub>Cl<sub>6</sub> and (b) (DPP-Py)Pb<sub>2</sub>Br<sub>6</sub> along the *c* axis (left) and *a* axis (right). Color code: C (black), H (cyan), N (blue), O (red), PbCl<sub>7</sub> (turquoise octahedra), PbBr<sub>7</sub> (grey octahedra).

network involve the methylpyridinium units, leading to a 1D chain of face-sharing octahedra similar to the one observed in the previously reported compound (MV)Pb<sub>2</sub>I<sub>6</sub> based on the methyl-viologen (MV<sup>2+</sup>) cation.<sup>11</sup>

Finally, the lead-free compound (DPP-Py)BiBr<sub>5</sub> crystallized as a perovskite-type (corner-sharing) 1D network of *cis*-connected octahedra (Fig. 4). As for the related lead-chloride and lead-bromide compounds, the main intermolecular interaction between cation and inorganic network involve the pyrrole units and apical Br atoms, with an N...Br distance of 3.303 Å. The stack of organic cations along the *c* axis show a 90° rotation between adjacent molecules, still strong  $\pi$ – $\pi$  interactions are highlighted by a distance between adjacent aromatic units of 3.654 Å.

### Spectroscopic properties and electronic structures

The purity of the polycrystalline powders for (DPP-Py)Pb<sub>2</sub>Cl<sub>6</sub>, (DPP-Py)Pb<sub>2</sub>Br<sub>6</sub>, (DPP-Py)Pb<sub>2</sub>I<sub>6</sub>(DMF)<sub>2</sub> and (DPP-Py)BiBr<sub>5</sub> was confirmed by powder X-ray diffraction (Fig. S8–S11). UV-Vis absorption measurements were performed on both powder samples and the pressed pellets further used for photoconductivity studies (Fig. 5a and Fig. S12). For powder samples, *E<sub>g</sub>* values range from 1.71 eV for (DPP-Py)BiBr<sub>5</sub> to 1.49 eV in (DPP-Py)Pb<sub>2</sub>I<sub>6</sub>(DMF)<sub>2</sub> (Fig. S13). These *E<sub>g</sub>* values are lower than those observed in previously reported hybrid CT compounds based on lead-iodide networks and viologen cation or bismuth-iodide and 4-methyl-piperidine cation<sup>37</sup> derivatives of type I architectures, suggesting that the DPP-based cation can efficiently involve CT with iodide-free compounds. After fabrication of the pressed pellets, these values were slightly lowered, particularly in (DPP-Py)BiBr<sub>5</sub> (from 1.71 eV in the

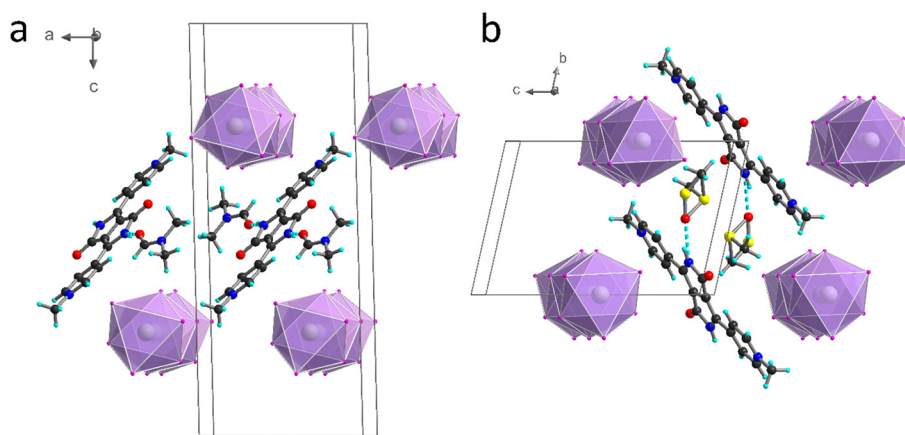


**Fig. 3** Crystal structures of (a) (DPP-Py) $\text{Pb}_2\text{I}_6\cdot\text{DMF}$  and (b) (DPP-Py) $\text{Pb}_2\text{I}_6\cdot\text{DMSO}$ . Color code: C (black), H (cyan), N (blue), O (red), S (yellow),  $\text{PbI}_6$  (purple octahedra), N–H...O bonding (cyan dashed lines).

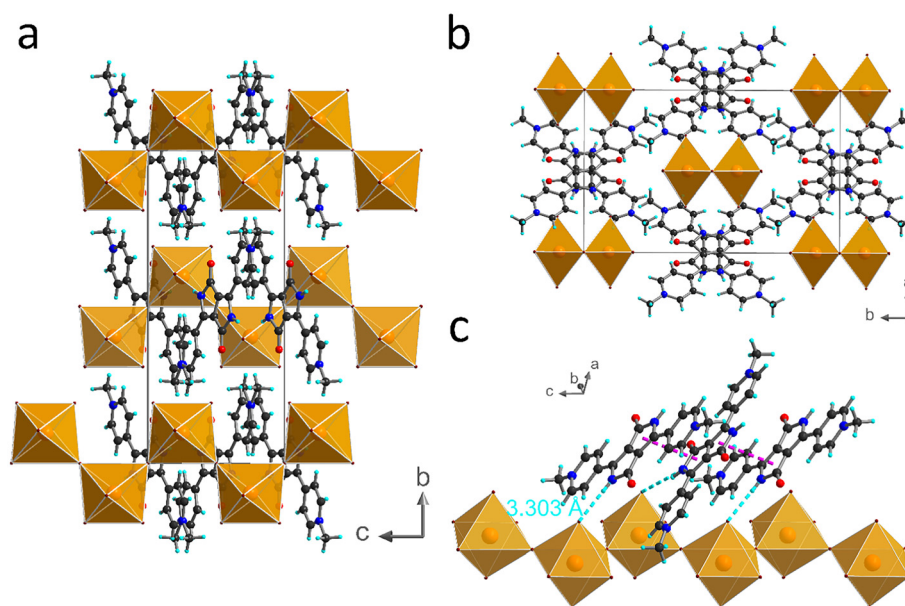


**Fig. 4** Crystal structure of (DPP-Py) $\text{BiBr}_5$ . (a) View along the *c* axis. (b) View along the *a* axis. (c) Intermolecular interactions between cation and inorganic chain. Color code: C (black), H (cyan), N (blue), O (red),  $\text{BiBr}_5$  (orange octahedra), N–H...O bonding (cyan dashed lines),  $\pi$ – $\pi$  stacking (pink dashed lines).

powder to 1.58 eV, see Fig. S14). Finally, the valence band energy was estimated by PESA measurements on pressed pellets and revealed a work function ranging from 5.83 to 5.88 eV being very similar for the four hybrid materials (Fig. S15). To gain deeper insight into the electronic structure of the DPP-Py based materials, we employed DFT (see SI for computational details). The computed band gaps recover the experimental trends with nearly identical gaps for (DPP-Py) $\text{Pb}_2\text{Cl}_6$  and (DPP-Py) $\text{Pb}_2\text{Br}_6$ , a slightly lower band gap for (DPP-Py) $\text{Pb}_2\text{I}_6\cdot\text{DMF}$ , and a greater band gap for (DPP-Py) $\text{Bi}_2\text{Br}_5$  (Fig. 5c–f and Table S3). The band structures of all compounds show similar features at the bottom conduction bands held by the DPP-Py organic cations. These molecular-like states show weak

dispersion across the Brillouin zone, making it difficult to characterize the nature of the band gap between direct or indirect. Such molecular states usually give sizable difference between the optical and electronic band gaps. Interestingly, the molecular calculation shows that this difference is around 0.27 eV for the DPP-Py cation (Fig. S16). When reporting this raw evaluation of the shift on the computed band gaps, we find an excellent agreement with the spectroscopic results. If the conduction bands are similar for all materials, the situation is different for the valence bands showing two distinct behaviors. (DPP-Py) $\text{Pb}_2\text{Cl}_6$  and (DPP-Py) $\text{Pb}_2\text{Br}_6$  present valence band tops built from contributions of the DPP-Py organic cations, while the VBM of (DPP-Py) $\text{Pb}_2\text{I}_6\cdot\text{DMF}$  and (DPP-Py)

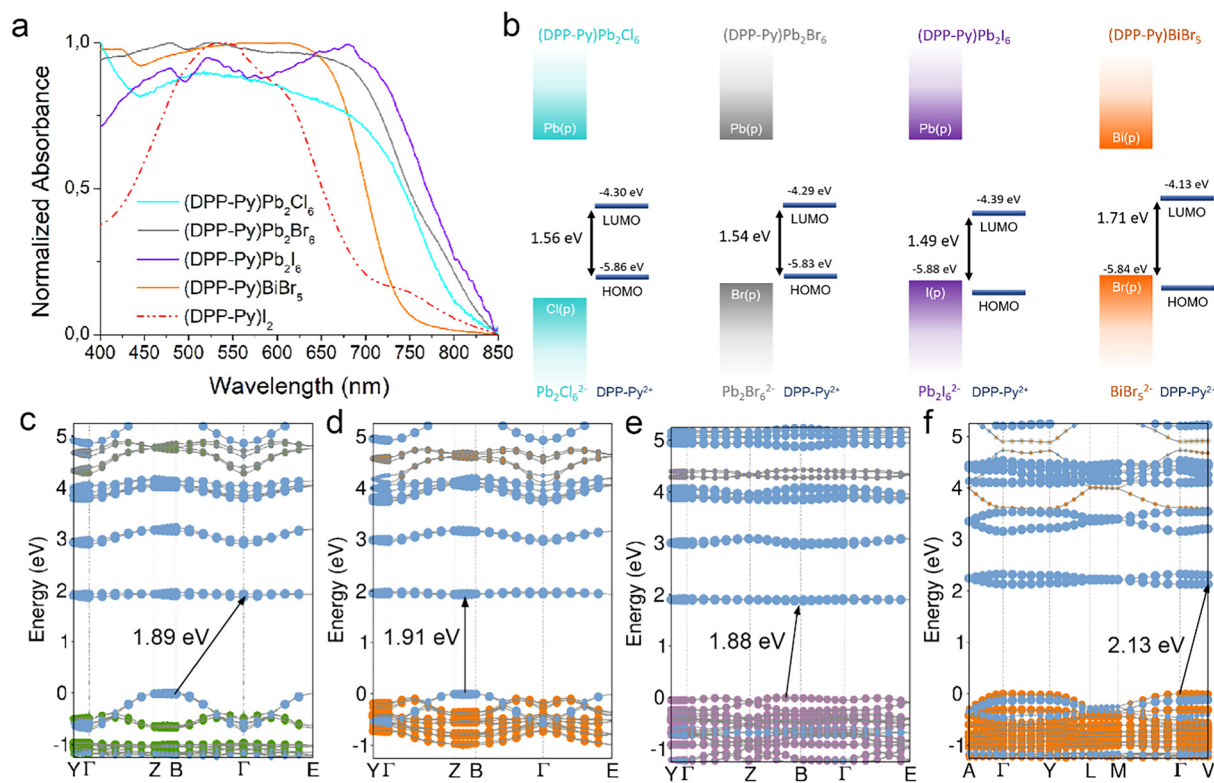


**Fig. 5** (a) UV-Vis absorption measurements on polycrystalline powders of the hybrid metal–halide compounds. (b) Proposed schematic energy diagram for (DPP-Py)Pb<sub>2</sub>Cl<sub>6</sub>, (DPP-Py)Pb<sub>2</sub>Br<sub>6</sub>, (DPP-Py)Pb<sub>2</sub>I<sub>6</sub>-DMF and (DPP-Py)BiBr<sub>5</sub> based on PESA measurements, UV-Vis absorption ( $E_g$  values for powder samples were considered) and the DFT computed band structure of (c) (DPP-Py)Pb<sub>2</sub>Cl<sub>6</sub>, (d) (DPP-Py)Pb<sub>2</sub>Br<sub>6</sub>, (e) (DPP-Py)Pb<sub>2</sub>I<sub>6</sub>-DMF and (f) (DPP-Py)BiBr<sub>5</sub>. The conduction bands are rigidly shifted so that the band gaps match the values obtained after correction by the PBE0 hybrid functional (see computational details). Gray, orange, green, and violet circles mark the contributions from the orbitals of Pb, Br, Cl, and I, respectively, while blue circles indicate the contributions of the DPP-Py<sup>2+</sup> cation.

BiBr<sub>5</sub> arise from the inorganic network (Fig. 6). In general, all the compounds present modest valence band dispersions, the best situation being obtained when the corner-shared BiBr<sub>5</sub> inorganic network is involved (Table S4). Based on UV-Vis absorption, PESA measurements and theoretical calculations,

an energy diagram was proposed for each compound (Fig. 5b). The three investigated lead-based hybrids show similar bandgap according to UV-Vis absorption measurements, however theoretical calculations highlighted the different types of alignments in their respective electronic structures

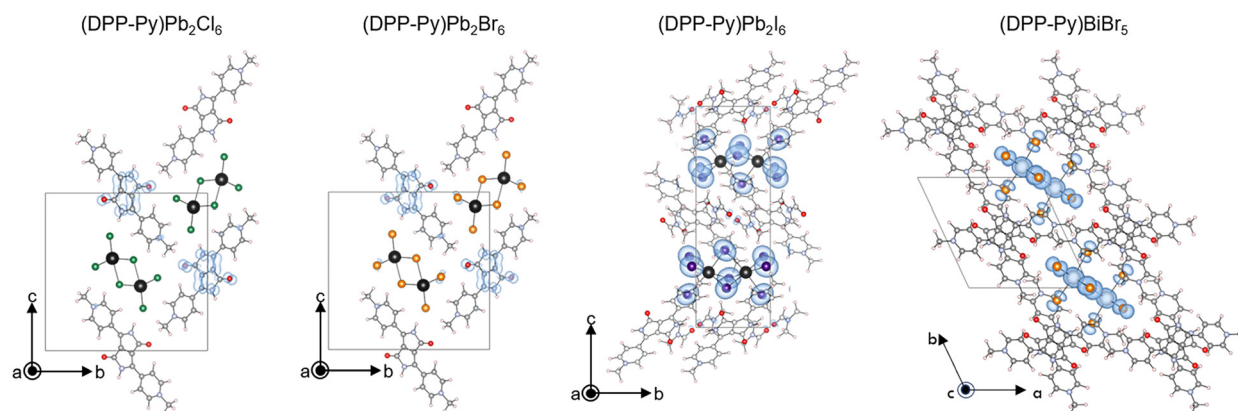


**Fig. 6** DFT computed partial charge density taken at the valence band maximum of (DPP-Py)Pb<sub>2</sub>Cl<sub>6</sub>, (DPP-Py)Pb<sub>2</sub>Br<sub>6</sub>, (DPP-Py)Pb<sub>2</sub>I<sub>6</sub>-DMF and (DPP-Py)BiBr<sub>5</sub>. The VBM of (DPP-Py)Pb<sub>2</sub>Cl<sub>6</sub> and (DPP-Py)Pb<sub>2</sub>Br<sub>6</sub> are distributed over the organic cations, while the VBM of (DPP-Py)Pb<sub>2</sub>I<sub>6</sub>-DMF and (DPP-Py)BiBr<sub>5</sub> involve the inorganic network.

induced by the electron character of the DPP-Py salt, from type I all organic for lead-chloride and lead-bromide to type II inorganic-organic CT architectures for lead-iodide. On the other hand, the bandgap opening of the cation together with the reduced bandgap in the inorganic part resulted in a different scenario in the case of the lead-free (DPP-Py)BiBr<sub>5</sub> material, *i.e.* a type II inorganic-organic CT energy alignment with a slightly higher, still promising bandgap for applications of CT hybrids. Although the CT could not be quantified with more advanced spectroscopy techniques, such as transient absorption and emission measurements due to film processing and photoluminescence quenching of the cation in the solid state, these

preliminary results clearly highlight the interest of these new class on cations in hybrid metal-halides. The use of DPP-Py instead of MV cations allows to strongly reduce the bandgap, as highlighted on (DPP-Py)Pb<sub>2</sub>I<sub>6</sub>-DMF with respect to previously reported (MV)Pb<sub>2</sub>I<sub>6</sub> and (HyEtV)Pb<sub>2</sub>I<sub>6</sub> compounds (Fig. S17), and on the lead-free (DPP-Py)BiBr<sub>5</sub> versus (MV)BiBr<sub>5</sub> (experimental  $E_g$  values of 1.71 and about 2 eV, respectively).<sup>8</sup> Our findings show the importance of the choice of cationic acceptor beside the supramolecular organization for bandgap tuning. Therefore, DPP-Py-based hybrids appear as promising candidates for the fabrication of photodetectors, particularly iodide and lead-free.

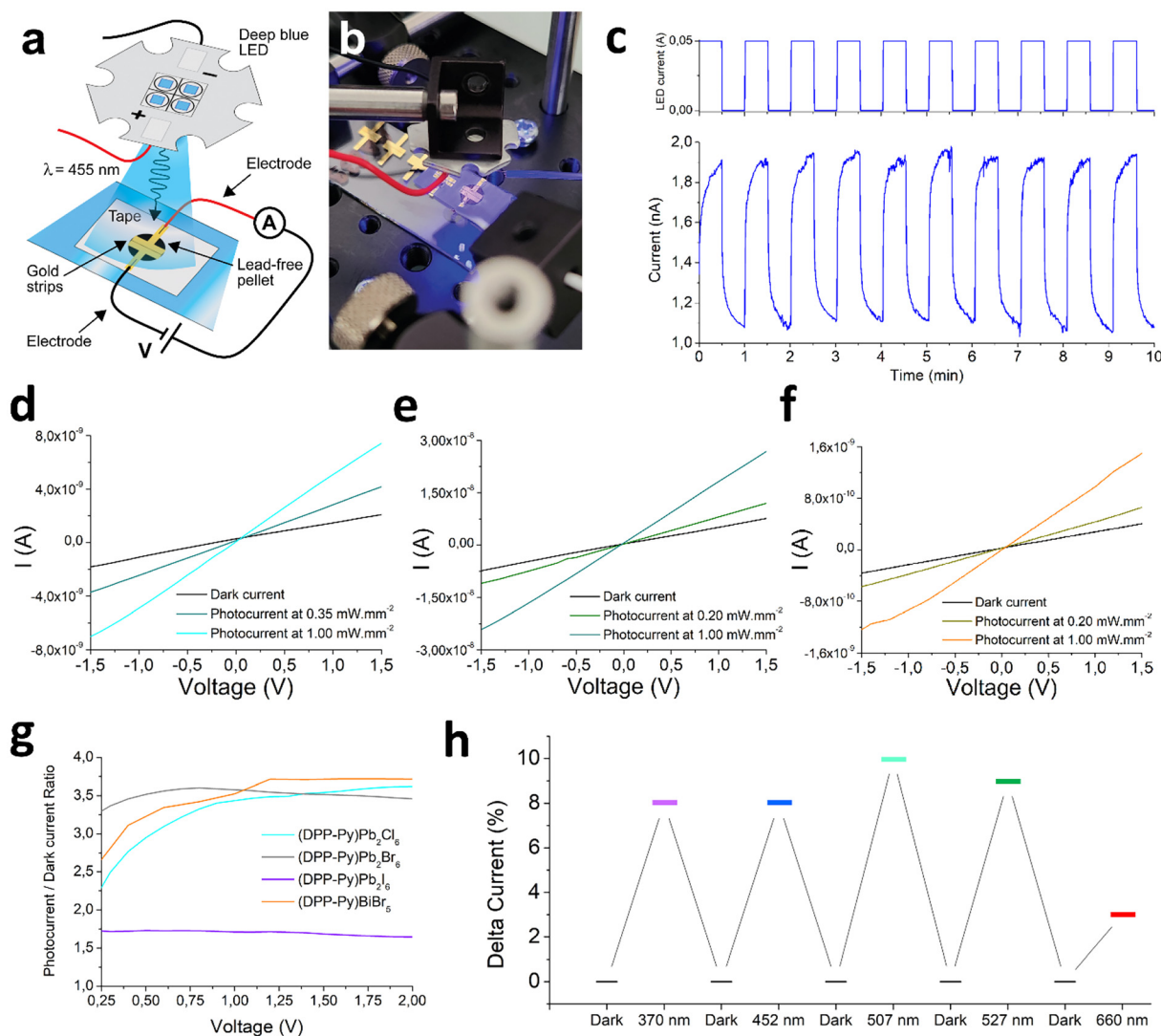


**Fig. 7** Photoconductivity measurements. (a) Schematic representation of the experimental setup. A hybrid metal-halide pellet is placed under a calibrated high-power LED capable of delivering 1 mW mm<sup>-2</sup> of monochromatic irradiation in deep blue (452 nm). (b) Photograph of the experimental setup. For clarity purpose the blue irradiation is set to minimum. (c) Time-dependent current responses of (DPP-Py)Pb<sub>2</sub>Cl<sub>6</sub> upon on/off cycles of 30 s, at -2.0 bias voltage. *I*-*V* characteristics of (d) (DPP-Py)Pb<sub>2</sub>Cl<sub>6</sub>, (e) (DPP-Py)Pb<sub>2</sub>Br<sub>6</sub> and (f) (DPP-Py)BiBr<sub>5</sub>. (g) Ratio between photocurrent and dark current values for (DPP-Py)Pb<sub>2</sub>Cl<sub>6</sub>, (DPP-Py)Pb<sub>2</sub>Br<sub>6</sub>, (DPP-Py)Pb<sub>2</sub>I<sub>6</sub>-DMF and (DPP-Py)BiBr<sub>5</sub>. (h) Increase (in %) of current response for (DPP-Py)Pb<sub>2</sub>Cl<sub>6</sub> upon irradiation with UV (370 nm), blue (452 nm), cyan (507 nm), green (527 nm) and red (660 nm) LEDs. For each color, an irradiance of 100 W m<sup>-2</sup> was selected.

## Photoconducting devices

Each one of the new hybrid metal–halides were evaluated for photoconductivity. Gold (Au) was evaporated on both ends of the pellet to act as contact electrodes, electrode thickness: 100 nm, space between electrodes: 100  $\mu\text{m}$  (Fig. S18). The DC input was increased stepwise from  $-1.5$  to  $+1.5$  V and subsequent currents were measured. A deep-blue (452 nm) calibrated high-power LED was used to perform  $I$ - $V$  characteristics under light (maximum intensity 1 mW  $\text{mm}^{-2}$ ). The observed linear  $I$ - $V$  curves indicate the ohmic behavior of the pellets and the Au electrodes, with measured current values for (DPP-Py) $\text{Pb}_2\text{I}_6(\text{DMF})_2$ , (DPP-Py) $\text{Pb}_2\text{Br}_6$ , (DPP-Py) $\text{Pb}_2\text{Cl}_6$  and (DPP-Py) $\text{BiBr}_5$  at 1.5 V of 9.4  $\mu\text{A}$ , 27.0 nA, 7.4 nA and 1.5 nA, respectively (Fig. 7 and Fig. S19). Thus, the higher current value at a given voltage of the (DPP-Py) $\text{Pb}_2\text{I}_6(\text{DMF})_2$  when compared with other three devices confirms the higher conductivity of the lead-iodide system, which was suggested from UV-Vis absorption measurements and calculated gap energy. Moreover, the performances of the (DPP-Py) $\text{BiBr}_5$  are similar to devices based on 1D lead-iodide inorganic networks with viologen cation with spacing of 80 and 180  $\mu\text{m}$ , and on Bi-iodide network with 4-methylpiperidine cation with spacing of 180  $\mu\text{m}$ <sup>37</sup> between the gold electrodes. These results are further confirming the interest of using electron-withdrawing cations in iodide-free materials as possible strategy for tuning the charge-transfer process and enhance photoconductivity. All compounds show photoconducting behavior, and the evolution in photocurrent/dark current ratio across the four systems follows the opposite trend with ratio values of up to 1.6, 3.5, 3.6 and 3.7 (at 1.0 mW  $\text{mm}^{-2}$ ) for (DPP-Py) $\text{Pb}_2\text{I}_6(\text{DMF})_2$ , (DPP-Py) $\text{Pb}_2\text{Br}_6$ , (DPP-Py) $\text{Pb}_2\text{Cl}_6$  and (DPP-Py) $\text{BiBr}_5$ , respectively (Fig. 7g). The stability of the materials could be confirmed by testing the photoconductivity on the same devices seven months after the first series of measurements on (DPP-Py) $\text{Pb}_2\text{Cl}_6$  and (DPP-Py) $\text{BiBr}_5$ , yielding similar results (Fig. S20). This was also supported by PXRD measurements on the (DPP-Py) $\text{Pb}_2\text{Cl}_6$  device which confirmed that the material could retain its crystallinity (Fig. S8), further highlighting their stability in air (under minimum 60% RH conditions) and over time. Moreover, the stability of the signal is highlighted by time-dependent current responses upon repeated on/off irradiation on (DPP-Py) $\text{Pb}_2\text{Cl}_6$ , suggesting the overall stability of the device under working conditions (Fig. 7c). Finally, the photodetection of the hybrid material upon different wavelengths of irradiation (with a fixed irradiance of 100 W  $\text{m}^{-2}$  for all colors) was probed (Fig. 7h). The similar photoresponse obtained using UV (370 nm), blue (452 nm), cyan (507 nm) and green (527 nm) LEDs, as well as a relatively small photoresponse under red light irradiation (660 nm), revealed a detection range for these materials spanning a large part of the visible spectrum. It should be noted the similar photoresponse observed in compounds showing an energy level alignment of type I (all-organic) and type II (organic–inorganic). Nevertheless, even in type I all-organic systems, the (photo)conducting behavior should be attributed to the hybrid nature

of the material. Indeed, a similar device constructed from the organic precursor alone (DPP-Py) $\text{I}_2$  revealed a very weak current response (of few pA under 1.5 V bias voltage) and the absence of photoconductivity under irradiation at 452 nm (Fig. S21).

## Conclusions

In summary, a DPP-based cation could be inserted in a series of 1D hybrid metal–halide compounds. The DPP-Py<sup>2+</sup> cation is readily available in two steps only, from commercially available reagents and presents other advantages such as redshift of the absorption and lower LUMO thanks to its electron accepting core. The versatility in chemical composition and crystal structures obtained confirms the ability of this organic molecule to combine with metal–halides in order to achieve CT materials. UV-Vis absorption and PESA measurements revealed the potential of such hybrids for the fabrication of photoconducting devices. For the same inorganic network, changing the nature of the cation from MV<sup>2+</sup> to DPP-Py<sup>2+</sup> allowed to tune the gap from 2.1 eV (previously reported in (MV) $\text{Pb}_2\text{I}_6$ ) to 1.49 eV (in (DPP-Py) $\text{Pb}_2\text{I}_6(\text{DMF})_2$ ). Moreover, one lead-free material, (DPP-Py) $\text{BiBr}_5$ , has values of 1.74 eV, similar to previously published photoconductor (HyEtV) $\text{Pb}_2\text{I}_6$  but lower than the only reported 1D (MV) $\text{BiBr}_5$  (around 2 eV). Theoretical calculations revealed the fine tuning of the electronic structure in the new series of compounds, ranging from a type I (all organic) alignment in the lead-chloride and lead-bromide networks, to a type II (organic–inorganic CT) hybrid in the bismuth-bromide material. Photoconducting devices were prepared and the measurements show photocurrent/dark current response ratios increasing from the lead-iodide to the bismuth-bromide systems. Our findings suggest the possibility to use small UV-Vis absorbing chromophores to fine tune the energy gap of CT hybrid metal–halide materials. We show for the first time that integration of the DPP chromophore into metal–halides allows to replace both lead ions and iodide anions by more eco-friendly and stable precursors, as highlighted by the performances of the bismuth-bromide network.

## Author contributions

T. F.: investigation, data curation. M. K.: investigation, data curation, software, validation. C. W.: investigation, data curation. A. R. K. and M. K.: data curation, investigation, software, validation. A. A. and F. P.: conceptualization, methodology, supervision, data curation, validation, writing – original draft, writing – review and editing. All authors have given approval to the final version of the manuscript.

## Conflicts of interest

There are no conflicts to declare.

## Data availability

The data supporting this article have been included as part of the supplementary information (SI). Supplementary information: experimental section, crystallographic data for the resolved structures,  $^1\text{H}$  NMR spectrum of (DPP-Py) $\text{I}_2$ , additional figures of crystal structures, PXRD of the polycrystalline powders, UV-Vis absorption measurements on pressed pellets, optical absorption of polycrystalline powders and pressed pellets, computational details and additional figures, pictures of the gold contacts,  $I$ - $V$  characteristics of the lead-iodide compound and of (DPP-Py) $\text{I}_2$ . See DOI: <https://doi.org/10.1039/d6qi00231e>.

CCDC 2494685–2494692 contain the supplementary crystallographic data for this paper.<sup>38a–h</sup>

## Acknowledgements

This work was supported by the CNRS, the University of Angers and the project “*Etoiles Montantes*” from *Région Pays la Loire* (CHAOS project). A. R. K. and C. K. acknowledge support from *Région Bretagne*, France through a SAD PEROPERE grant. This work was granted access to the HPC resources of CINES and TGCC under the allocation 2026-A0190907682 made by GENCI.

## References

- N. Arora, M. I. Dar, A. Hinderhofer, N. Pellet, F. Schreiber, S. M. Zakeeruddin and M. Grätzel, Perovskite solar cells with CuSCN hole extraction layers yield stabilized efficiencies greater than 20%, *Science*, 2017, **358**, 768–771.
- B. Saparov and D. Mitzi, Organic-Inorganic Perovskites: Structural Versatility for Functional Materials Design, *Chem. Rev.*, 2016, **116**, 4558–4596.
- C. Katan, N. Mercier and J. Even, Quantum and Dielectric Confinement Effects in Lower-Dimensional Hybrid Perovskite Semiconductors, *Chem. Rev.*, 2019, **119**, 3140–3192.
- H. Tsai, W. Nie, J.-C. Blancon, C. C. Stoumpos, C. M. M. Soe, J. Yoo, J. Crochet, S. Tretiak, J. Even, A. Sadhanala, G. Azzellino, R. Brenes, P. M. Ajayan, V. Bulović, S. D. Stranks, R. H. Friend, M. C. Kanatzidis and A. D. Mohite, Stable Light-Emitting Diodes Using Phase-Pure Ruddlesden-Popper Layered Perovskites, *Adv. Mater.*, 2018, **30**, 1704217.
- J. Kim, J. Lee, J.-M. Lee, A. Facchetti, T. J. Marks and S. K. Park, Recent Advances in Low-Dimensional Nanomaterials for Photodetectors, *Small Methods*, 2024, **8**, 2300246.
- S. Nussbaum, D. Tsokkou, A. T. Frei, D. Friedrich, J.-E. Moser, N. Banerji, J.-H. Yum and K. Sivula, Free Charge Carrier Generation by Visible-Light-Absorbing Organic Spacers in Ruddlesden–Popper Layered Perovskites, *J. Am. Chem. Soc.*, 2024, **146**, 27770–27778.
- R. Hooijer, S. Wang, A. Biewald, C. Eckel, M. Righetto, M. Chen, Z. Xu, D. Blätte, D. Han, H. Ebert, L. M. Herz, R. T. Weitz, A. Hartschuh and T. Bein, Overcoming Intrinsic Quantum Confinement and Ultrafast Self-Trapping in Ag–Bi–I- and Cu–Bi–I-Based 2D Double Perovskites through Electroactive Cations, *J. Am. Chem. Soc.*, 2024, **146**, 26694–26706.
- J. Sun, K. Wang, K. Ma, J. Y. Park, Z.-Y. Lin, B. M. Savoie and L. Dou, Emerging Two-Dimensional Organic Semiconductor-Incorporated Perovskites – A Fascinating Family of Hybrid Electronic Materials, *J. Am. Chem. Soc.*, 2023, **145**, 20694–20715.
- E. Amerling, Y. Zhai, B. W. Larson, Y. Yao, B. Fluegel, Z. Owczarczyk, H. Lu, L. Whittaker-Brooks, V. Blum and J. L. Blackburn, Charge transfer states and carrier generation in 1D organolead iodide semiconductors, *J. Mater. Chem. A*, 2021, **9**, 14977–14990.
- H. Fang, F.-H. Chen, S.-Q. Zhang and M.-J. Lin, Three Semiconductive 1D Naphthalene Diimide/Iodoplumbate Perovskites with High Moisture Tolerance and Long-Lived Charge Separation States, *Inorg. Chem.*, 2023, **62**, 9661–9670.
- Y. Gao, E. Shi, S. Deng, S. B. Shiring, J. M. Snider, C. Liang, B. Yuan, R. Song, S. M. Janke, A. Liebman-Peláez, P. Yoo, M. Zeller, B. W. Boudouris, P. Liao, C. Zhu, V. Blum, Y. Yu, B. M. Savoie, L. Huang and L. Dou, Molecular Engineering of Organic–Inorganic Hybrid Perovskites Quantum Wells, *Nat. Chem.*, 2019, **11**, 1151–1157.
- W. Bi, N. Leblanc, N. Mercier, P. Auban-Senzier and C. Pasquier, Thermally Induced Bi(III) Lone Pair Stereoactivity: Ferroelectric Phase Transition and Semiconducting Properties of (MV)BiBr<sub>5</sub> (MV= methylviologen), *Chem. Mater.*, 2009, **21**, 4099–4101.
- N. Leblanc, W. Bi, N. Mercier, P. Auban-Senzier and C. Pasquier, Photochromism, Electrical Properties, and Structural Investigations of a Series of Hydrated Methylviologen Halobismuthate Hybrids: Influence of the Anionic Oligomer Size and Iodide Doping on the Photoinduced Properties and on the Dehydration Process, *Inorg. Chem.*, 2010, **49**, 5824–5833.
- N. Leblanc, N. Mercier, M. Allain, O. Toma, P. Auban-Senzier and C. Pasquier, The motley family of polar compounds (MV)[M(X<sub>5</sub>–xX'<sub>x</sub>)] based on anionic chains of *trans*-connected M(III)(X,X')<sub>6</sub> octahedra (M=Bi, Sb; X, X'=Cl, Br, I) and methylviologen (MV) dications, *J. Solid State Chem.*, 2012, **195**, 140–148.
- J.-I. Fujisawa and T. Ishihara, Charge-transfer transitions between wires and spacers in an inorganic-organic quasi-one-dimensional crystal methylviologen lead iodide, *Phys. Rev. B:Condens. Matter Mater. Phys.*, 2004, **70**, 113203.
- J.-I. Fujisawa and G. Giorgi, Lead-iodide nanowire perovskite with methylviologen showing interfacial charge-transfer absorption: a DFT analysis, *Phys. Chem. Chem. Phys.*, 2014, **16**, 17955–17959.

- 17 B. Febriansyah, T. M. Koh, R. A. John, R. Ganguly, Y. Li, A. Bruno, S. G. Mhaisalkar and J. England, Inducing Panchromatic Absorption and Photoconductivity in Polycrystalline Molecular 1D Lead-Iodide Perovskites through  $\pi$ -Stacked Viologens, *Chem. Mater.*, 2018, **30**, 5827–5830.
- 18 R. P. Reynolds, J. H. Persaud, G. Volonakis, A. J. Torma, P. E. Meza, Z. E. Kelly, C. C. Stoumpos, V. P. Dravid, C. Katan, A. D. Mohite and M. G. Kanatzidis, Design Principles for Narrow-Gap Hybrid Semiconductors: Insights from Viologen-Tin and Viologen-Lead Iodides, *J. Am. Chem. Soc.*, 2025, **147**, 24573–24593.
- 19 E. S. Vasileiadou, I. Hadar, M. Kepenekian, J. Even, Q. Tu, C. D. Malliakas, D. Friedrich, I. Spanopoulos, J. M. Hoffman, V. P. Dravid and M. G. Kanatzidis, Shedding Light on the Stability and Structure–Property Relationships of Two-Dimensional Hybrid Lead Bromide Perovskites, *Chem. Mater.*, 2021, **33**, 5085–5107.
- 20 M. A. Naik and S. Patil, Diketopyrrolopyrrole-based conjugated polymers and small molecules for organic ambipolar transistors and solar cells, *J. Polym. Sci., Part A: Polym. Chem.*, 2013, **51**, 4241–4260.
- 21 S. Wang, M. Zhao, D. Jiang, T. Tiang and J. Huang, Bias-Switchable Dual-Mode Organic–Inorganic Composite Photodetector with Tunable Spectral Response, *ACS Mater. Lett.*, 2025, **7**, 3074–3081.
- 22 N. Luo, G. Zhang and Z. Liu, Keep glowing and going: recent progress in diketopyrrolopyrrole synthesis towards organic optoelectronic materials, *Org. Chem. Front.*, 2021, **8**, 4560–4581.
- 23 J. Humphreys, F. Malagrecia, P. A. Hume, E. S. Davies, S. P. Argent, T. D. Bradshaw and D. B. Amabilino, Highly electron deficient diketopyrrolopyrroles, *Chem. Commun.*, 2023, **59**, 1613–1616.
- 24 S. Jenni, F. Ponsot, P. Baroux, L. Collard, T. Ikeno, K. Hanaoka, V. Quesneau, K. Renault and A. Romieu, Design, synthesis and evaluation of enzyme-responsive fluorogenic probes based on pyridine-flanked diketopyrrolopyrrole dyes, *Spectrochim. Acta, Part A*, 2021, **248**, 119179.
- 25 W. Xu, J. Wang, C. Xu, J. Hua and Y. Wang, A diketopyrrolopyrrole-based ratiometric fluorescent probe for endogenous leucine aminopeptidase detecting and imaging with specific phototoxicity in tumor cells, *J. Mater. Chem. B*, 2021, **9**, 8842–8850.
- 26 J. Wang, L. Liu, W. Xu, Z. Yang, Y. Yan, X. Xie, Y. Wang, T. Yi, C. Wang and J. Hua, Mitochondria-Targeted Ratiometric Fluorescent Probe Based on Diketopyrrolopyrrole for Detecting and Imaging of Endogenous Superoxide Anion in Vitro and in Vivo, *Anal. Chem.*, 2019, **91**, 5786–5793.
- 27 J. Wang, W. Xu, Z. Yang, Y. Yan, X. Xie, N. Qu, Y. Wang, C. Wang and J. Hua, New Diketopyrrolopyrrole-Based Ratiometric Fluorescent Probe for Intracellular Esterase Detection and Discrimination of Live and Dead Cells in Different Fluorescence Channels, *ACS Appl. Mater. Interfaces*, 2018, **10**, 31088–31095.
- 28 J. Mizuguchi, A. Iqbal and G. Giller, Preparation of electrochromic diketopyrroles for electrochromic display devices, DE4435211A1, 1995.
- 29 C. Liu, Z. Fang, J. Sun, M. Shang, K. Zheng, W. Yang and Z. Ge, Donor-acceptor-donor type organic spacer for regulating the quantum wells of Dion-Jacobson 2D perovskites, *Nano Energy*, 2022, **93**, 106800.
- 30 G. H. Schoenmakers, R. Waagenaar and J. J. Kelly, Methylviologen Redox Reactions at Semiconductor Single Crystal Electrodes, *Phys. Chem.*, 1996, **100**, 1169–1175.
- 31 H. Ftouni, F. Bolze and J. Nicoud, Water-soluble diketopyrrolopyrrole derivatives for two-photon excited fluorescence microscopy, *Dyes Pigm.*, 2013, **97**, 77–83.
- 32 C. Elliot, J. A. McNulty, D. B. Cordes, A. M. Z. Slawin and P. Lightfoot, Structural diversity in hybrid lead halides templated by 4-methylimidazolium, *J. Solid State Chem.*, 2021, **303**, 122466.
- 33 S.-P. Zhao, Q.-H. Yu, P. Yang, Y. Guo, J. Wang and H. Xu, Diverse structures and multi-step dielectric relaxation of three lead bromide hybrid crystals based on 1-aminopyridinium and its cyano-substituted Schiff bases, *Polyhedron*, 2022, **227**, 116121.
- 34 M. Krummer, N. Glissmann, B. Zimmermann, P. Klingenberg, M. Daub and H. Hillebrecht, Interactions of Pyridine-Based Organic Cations as Structure-Determining Factors in Perovskite-Related Compounds  $AxPb(II)yBrz$ , *Eur. J. Inorg. Chem.*, 2023, **26**, e202200671.
- 35 D. S. Shtarev, D. A. Chaplygina, O. V. Patrusheva, C. Chen, A. V. Shtareva, C. C. Stoumpos, R. Kevorkyants and A. V. Emeline, The effect of precursor concentrations on the structure and optoelectronic properties of quasi low-dimensional hybrid 2-methylpyridinium lead bromide crystalline phases, *J. Mater. Chem. C*, 2024, **12**, 5596–5607.
- 36 A. S. Chow, X. Zhong, D. H. Fabini, M. Zeller and C. M. Oertel,  $(C_5H_6N)Pb_2X_5$  ( $X = Cl, Br$ ): Hybrid Lead Halides Based on Seven-Coordinate Pb(II), *Inorg. Chem.*, 2022, **61**, 6530–6538.
- 37 W. Zhang, K. Tao, C. Ji, Z. Sun, S. Han, J. Zhang, Z. Wu and J. Luo,  $(C_6H_{13N})_2BiI_5$ : A One-Dimensional Lead-Free Perovskite-Derivative Photoconductive Light Absorber, *Inorg. Chem.*, 2018, **57**(8), 4239–4243.
- 38 (a) CCDC 2494685: Experimental Crystal Structure Determination, 2026, DOI: [10.5517/ccdc.csd.cc2pqxq2](https://doi.org/10.5517/ccdc.csd.cc2pqxq2); (b) CCDC 2494686: Experimental Crystal Structure Determination, 2026, DOI: [10.5517/ccdc.csd.cc2pqxr3](https://doi.org/10.5517/ccdc.csd.cc2pqxr3); (c) CCDC 2494687: Experimental Crystal Structure Determination, 2026, DOI: [10.5517/ccdc.csd.cc2pqxs4](https://doi.org/10.5517/ccdc.csd.cc2pqxs4); (d) CCDC 2494688: Experimental Crystal Structure Determination, 2026, DOI: [10.5517/ccdc.csd.cc2pqxt5](https://doi.org/10.5517/ccdc.csd.cc2pqxt5); (e) CCDC 2494689: Experimental Crystal Structure Determination, 2026, DOI: [10.5517/ccdc.csd.cc2pqxv6](https://doi.org/10.5517/ccdc.csd.cc2pqxv6); (f) CCDC 2494690: Experimental Crystal Structure Determination, 2026, DOI: [10.5517/ccdc.csd.cc2pqxw7](https://doi.org/10.5517/ccdc.csd.cc2pqxw7); (g) CCDC 2494691: Experimental Crystal Structure Determination, 2026, DOI: [10.5517/ccdc.csd.cc2pqxx8](https://doi.org/10.5517/ccdc.csd.cc2pqxx8); (h) CCDC 2494692: Experimental Crystal Structure Determination, 2026, DOI: [10.5517/ccdc.csd.cc2pqxy9](https://doi.org/10.5517/ccdc.csd.cc2pqxy9).